Shigeo Aoki, Sadatoshi Miura, Wataru Kawanbe, Shirou Matuda

Influence of Air Pollution on the Great Buddha in Kamakura

Introduction

The Tokyo National Research Institute of Cultural Properties (TNRICP) has studied the influence of environmental pollutants on outdoor cultural property made of metal since 1992. One of the objects of study thus selected is the Seated Image of Amida Nyorai (National Treasure) of Kotoku-in Temple in Kamakura (Fig. 1 and Table 1), which is commonly known as the Great Buddha in Kamakura. The reasons for selecting this image are:

1. this image is made of bronze, a typical copper alloy,
2. it has stood exposed to the open air for about five hundred years in Kamakura City,
3. Kamakura is about 50 km south of Tokyo, a location within easy reach of Tokyo,
4. there are also many other objects of cultural value in its surrounding area.

To study the relationship between the corrosion behavior of outdoor cultural property made of metal and the environmental conditions, the Institute has been analyzing the compositions and structures of corrosion products formed on the surface of the Great Buddha since 1992, while at the same time conducting exposure tests using imitation materials of the image, making meteorological observations and monitoring air pollution in the surrounding area.

Environmental Pollutants Around the Great Buddha

To study the influence of environmental pollutants on the Great Buddha in Kamakura, elution tests of contaminated gases, mist, acid precipitation, and exposure test samples were conducted in the precincts of this temple, Kotoku-in. Measurement started in January 1993.

1. Sulfur Dioxide (SO_2) and Nitrogen Dioxide (NO_2)

Method of Measurement

SO_2/NO_2 monitors (dia. 5 cm, height 2.5 cm) were exposed in places free from rainfall. After 30 days of exposure, the monitors were taken back and washed in ion exchange water. Their extract was then analyzed by ion chromatography.

Result of Measurement

Their concentrations after the exposure test period were shown in ppb.

Place of Measurement

Each monitor was exposed in an instrument shelter on the rooftop of the temple and in the body of the Great Buddha.

2. Chloride Ion (Cl^-), Nitric Acid Ion (NO_3^-), Sulfate Ion (SO_4^{2-}), Natrium Ion (Na^+), Ammonia Ion (NH_4^+) and Potassium Ion (K^+)

Method of Measurement

Gauze-type mist collectors (dia. 10 cm, surface area 157 cm^2) were exposed in places free from rainfall. After 30 days of exposure, the collectors were taken in and washed in ion exchange water. Their extract was then analyzed by ion chromatography.

Result of Measurement

The respective amounts of chloride ion (Cl^-), nitric acid ion (NO_3^-), sulfate ion (SO_4^{2-}), natrium ion (Na^+), ammonia ion (NH_4^+), and potassium ion (K^+) collected by the gauzes during the 30-day exposure period were shown in mg/157 cm^2.

Place of Measurement

Each collector was exposed in an instrument shelter on the rooftop of the temple and in the body of the Great Buddha.

3. Chloride Ion (Cl^-), Nitric Acid Ion (NO_3^-), Sulfate Ion (SO_4^{2-}), Natrium Ion (Na^+), Ammonia Ion (NH_4^+), Potassium Ion (K^+), Magnesium Ion (Mg^{2+}), and Calcium Ion (Ca^{2+}) during rainfalls

Method of Measurement

The rain collected by a rain collector for periods of 30 days each was analyzed by both ion chromatography and an inductively coupled plasma atomic emission spectrometer (ICP-AES Type SPS1200A manufactured by Seiko Instruments Inc.).

Result of Measurement

The amounts of ions collected for each period of 30 days were shown in mg.

Place of Measurement

The collector was set up on the rooftop of the temple.

4. Chloride Ion (Cl^-), Nitric Acid Ion (NO_3^-), Sulfate Ion (SO_4^{2-}), Natrium Ion (Na^+), Ammonia Ion (NH_4^+), and Potassium Ion (K^+) during one rainfall

Method of Measurement

The rain collected during each rainfall of 1 mm was analyzed. These ions were measured and analyzed by ion chromatography.

Table 1. Chronlogical Table

1252	The Great Buddha completed and this hall (Great Buddha Hall) constructed
1335	Great Buddha Hall destroyed by a typhoon
1369	Great Buddha Hall destroyed again by a typhon
1495	Great Buddha Hall washed away by a tsunami (tidal wave) and not reconstructed since then, leaving the Great Buddha outdoors
1923	The base of the Great Buddha destroyed by the Kanto Great Earthquake, and the image tilted a little to the front
1926	The base of the Great Buddha reinforced and its asaimatic structure repaired
1960	Large-scale restoration carried out: 1) The neck fixed with reinforced plastic 2) The base replaced by a stainless steel board
1922	TNRIP's preparatory study started
1995	TNRIP's main study started

Result of Measurement
The amounts of ions collected during one rainfall were shown in ppm.
Place of Measurement
The collector was set up on the rooftop of the temple.

5. Elution Test of a Bronze Plate
A bronze plate (4 x 3 cm, Cu 85%, Pb 5%, Zn 5%, Sn 5%) was subjected to exposure, and then its elution test was conducted.
Method of Measurement
The bronze plate was attached onto the south 45° slant of the tunnel in the collector. The rain that flowed down on the bronze plate was collected for periods of 30 days each. The rain was then analyzed by an ICP-AES (Type SPS1200A manufactured by Seiko Instruments Inc.) to measure the changes in weight of Cu^{2+}, Pb^{2+}, Sn^{2+}, and Zn^{2+}.
Result of Measurement
The changes in weight were shown in mg. The amounts of ions collected during the period of exposure were also shown in mg.
Place of Measurement
The rain collector was set up on the rooftop of the temple.

6. Elution Test of Marble
Method of Measurement
Pieces of marble (2.0 x 2.0 x 0.5 mm) were ultrasonic-cleaned and then subjected to exposure both outdoors (on the south 45° slant of the exposure stand) and indoors (hung in an instrument shelter).

After four months of exposure, they were taken back and ultrasonic-cleaned in 20 ml of pure water. The extracted water was analyzed by ion chromatography to measure the changes in weight of Cl^-, NO_3^-, SO_4^{2-}, Na^+, NH_4^+, and K^+ before and after exposure. Mg^{2+} and Ca^{2+} were analyzed with an IEC-AES.
Result of Measurement
The changes in weight of these ions were shown in mg. Their amounts were shown in ppm.

7. Results and Discussion
- The concentrations of NO_2 and SO_2 (quantitatively determined as SO_4^{2-}) in the atmosphere as observed in the simple monitors were found to undergo seasonal changes. The concentration of NO_2 has a tendency to become lower in summer.
- The concentrations of NO_3^- and SO_4^{2-} in mist were both remarkably high in summer. To put it differently, the concentration of contamination in mist tends to be higher in rainy months, while the concentrations of NO_3^- and SO_4^{2-} in mist tend to be lower in months of little rain. NO_2 and SO_2 were found to be just contrary to the two above in their tendency (Fig. 2).
- The anions and cations collected during rainfalls in each month were compared with each other. The result shows a remarkable regional feature, namely that the amount of Cl^- and correspondingly that of Na^+ are both greater in Kamakura than at the three other points outside Kamakura (Fig. 3).
- In Ueno, Tokyo, where TNRICP is located, rain in the initial stage of a rainfall is usually divided into two groups in pH value: one around 4 and the other around 7 on the pH scale. In contrast, it centered in the range of 4.0-5.5 in Kamakura (Kotoku-in Temple). On the whole, the EC value of rain in the initial stage of a rainfall was higher in Ueno. It has also been found that the EC value of the next rain has a tendency to become higher when rainless days continued for a long time. NO_3^- is considered to play a role as a factor of decreasing pH (Fig. 4).
- The elution amount of copper was found to be correlated with the amount of anions. The high amount of Cl^- shown in Figure 3 is due to the geographical feature of Kamakura which is located in a seaside district. It does not seem to be related to the elution of copper. The bronze plate is composed as described earlier, and Cu was in fact eluted in the greatest amount. The elements of the bronze plate were compared with each other by taking their composition ratios into account (taking the actual elution amount of Cu to be 1/17). As a result, it was found that Pb elution was most remarkable in the initial stage of exposure and that the elution amount of each element was in the order of Pb > Zn > Cu. After some months of exposure, Pb sharply decreased in elution amount to the extent that Zn got ahead of Pb in this respect. Sn was scarcely detected in the period of exposure from the initial stage (Fig. 5).
- All marble fragments decreased in weight, although there were differences depending on the location and the time of exposure. Marble ($CaCO_3$) is weak against acid. It is, therefore, considered to have been eluted by oxidized rain and also to have been affected by dry deposition. In fact, as the amount of anions in rain or mist increased, the result was a greater decrease in weight. This suggests that the decrease in weight of the marble was greatly affected not only by the elution effect of acid but also by water-soluble products generated by NO_3^- and SO_4^{2-} which stuck to the surface of the marble (NO_3^- and SO_4^{2-} are main substances that caused air pollution). The comparison between the decrease in weight of the marble fragments that were subjected to outdoor exposure and the amount of SO_4^{2-} that was extracted from the marble fragments exposed indoors in the same period revealed that as the amount of SO_4^{2-} increased, the decrease in weight of the marble fragments was greater. It can, therefore, be considered that the amount of SO_4^{2-} as a pollutant greatly affects marble (Fig. 6).

Wind Around the Great Buddha – Wind Direction and Wind Speed

Meteorological observations have been conducted in the surrounding area of the Great Buddha to look into its atmospheric corrosion.
The data include:
a) general weather condition in Kamakura City,
b) characteristics of the wind directions in and around Kamakura,
c) streams of wind around the Great Buddha.
Data available from the AMeDAS (Automated Meteorological Data Acquisition System) is used in addition to the results of our own observations. Item c) above was surveyed mainly by wind tunnel tests.

1. Characteristics of the Wind Directions in and around Kamakura
The frequencies of occurrence of the wind directions in and around Kamakura as shown in Table 2 were analyzed to examine the characteristics of the wind directions in Kamakura. The data analyzed here was obtained at the following six observation points.

Fig. 1. The Great Buddha in Kamakura

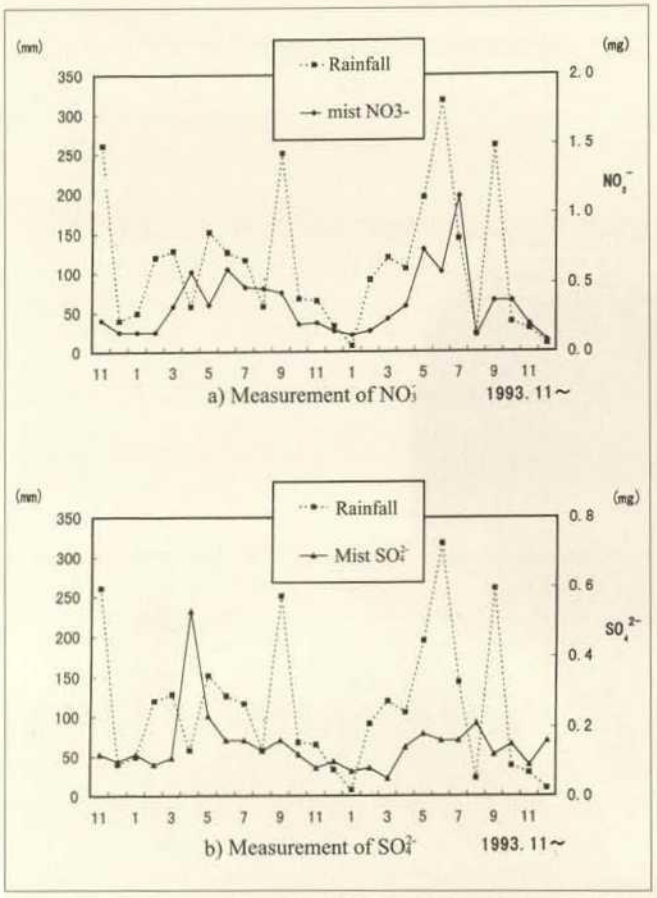

Fig. 2. The rainfall and mist contain NO^-_3 and SO^{2-}_4 at Kotoku-in Temple

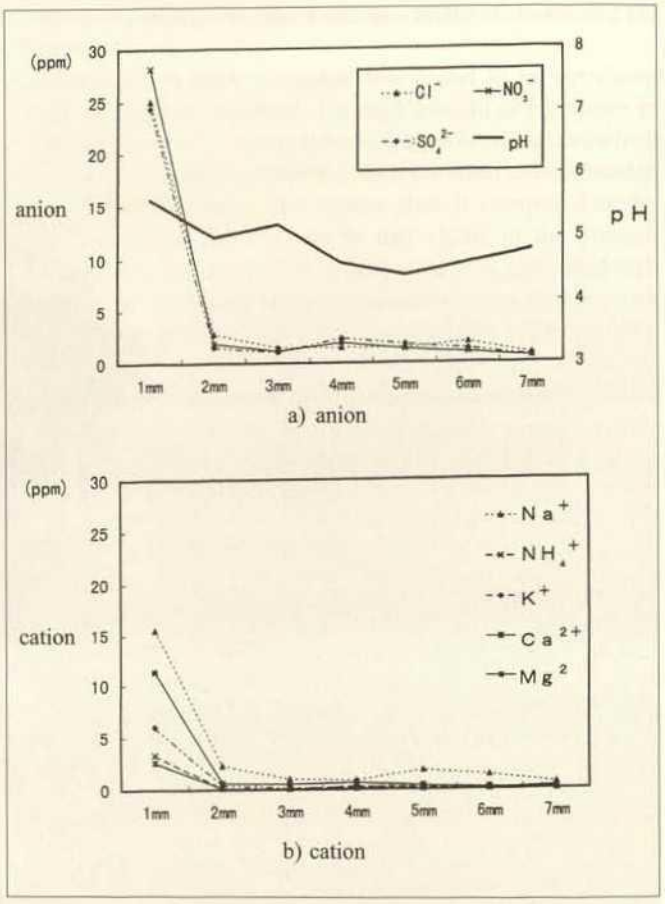

Fig. 4. The pH values of rainwater (1995.9.15) Kotoku-in Temple

Fig. 3. The amount of Cl^-, NO^-_3 and SO^{2-}_4 in the rainwater in each month

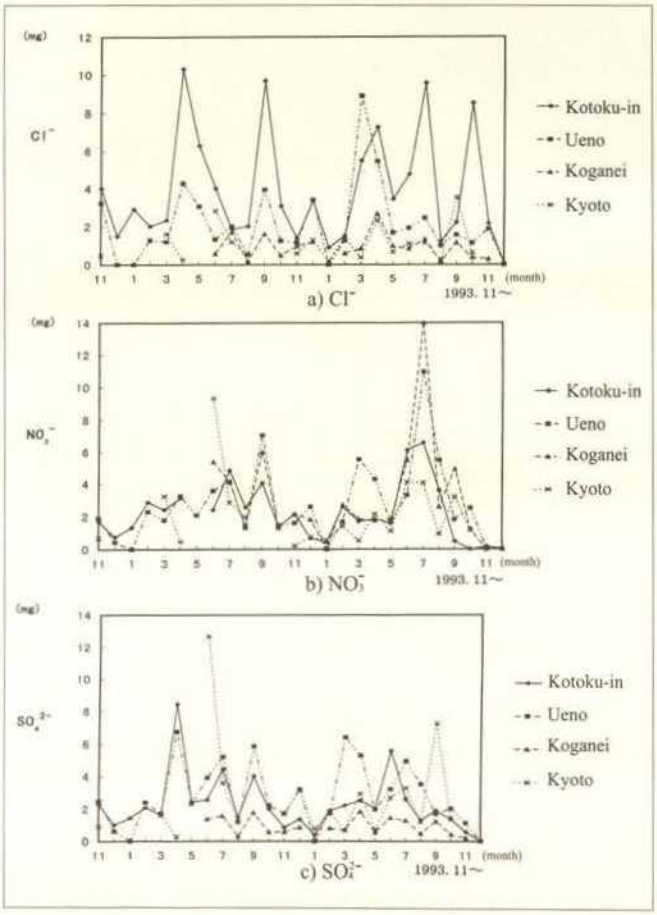

The frequencies of occurrence of wind directions refer to the way the wind blows at what rate in a certain district. For example, at the observation point in Yokohama, about 25% of the annual total winds are from the north. This result further reveals that the east side and the west side divided at the Miura Peninsula are slightly different in the characteristics of the wind directions and that the wind blows parallel to the north-south axis at a higher rate on the west side (Kamakura side). In the neighborhood of the Great Buddha (observation point 2), the wind blows parallel to the NNE-SSW axis at a higher rate due to the geographical features of the area.

Figure 7 shows the frequencies of occurrence of the wind directions during a rainfall of 1 mm or more or while blowing at a wind speed of 8 m/s or more at each of the three observation points (Yokohama, the Great Buddha 1 and 2). As shown in the figure, the north wind blows at a higher rate during such rainfalls, and the wind, when blowing hard, most frequently comes from the south.

Table 2. Observation Points

Observation Point	Yokohama	Ebina	Tsujido	Miura	Great Buddha 1	Great Buddha 2
Altitude (m)	39	18	5	42	42	11
Height ground level (m)	19.6	6.5	9.5	10	10	15

From these results it can be inferred that pollutants can easily be carried to the Great Buddha from the Tokyo-Yokohama industrial area by the north wind, while sea salt particles can also easily be carried from the sea by the strong south wind. This is considered to have affected the formation of corrosion products on the north and south sides of the Great Buddha.

2. Streams of Wind Around the Great Buddha

The streams of wind around the Great Buddha were investigated by two kinds of tunnel tests: visibility test using smoke and wind pressure measurement test. The tests were conducted by using a model prepared on a scale of 1:100. The following is a brief summary of what has been found out from these tests.

The NNW, N, and NNE winds are almost the same in their streams. Figure 8 shows the wind pressure distributions of the N and S winds. The wind pressure distribution here refers to the distribution of varying degrees of pressure acting on the surface of the Great Buddha. The positive value represents the pressure acting from the exterior to the interior, and the negative value the reverse. This means that, if there are openings or crevices on the surface, the wind blows in from the exterior at those spots where positive values are shown. This tendency becomes more prominent as the value increases. As shown in Figure 8 a, in the case of the N wind, the wind pressure value is positive on almost the entire area of the Great Buddha's back side, the side facing to windward, while the value is negative almost the entire area of the front. The same tendency is also seen in the S wind – the positive value on the front (windward side) and the negative value on the back side (leeward side). Compared with the N wind, the S wind is greater in wind pressure value, on the whole owing to the geographical conditions, as there are mountains on the windward side of the N wind. Consequently, those mountains serve as an obstacle to the flowing of the N wind. The S wind, on the other hand, has no such obstacle and can freely flow in.

What has been stated above, coupled with the result of our visibility tests using smoke, shows that, compared with the S wind, the N wind gently blows against the rear (windward side) of the Great Buddha and flows away leeward. There is also a tendency that its flow decreases in speed and becomes stagnant around the portion below about one fourth of the height of the image. The S wind, on the other, strongly blows against the front (windward side) of the Great Buddha and wraps round the image, flowing hard around its sides.

Fig. 5. The result of elution test of a bronze plate (this figure shows anion contained in the rainwater and the amount of bronze which began to melt from bronze plate)

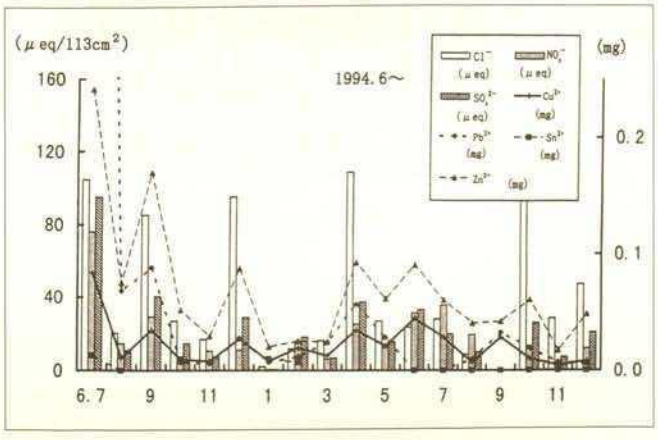

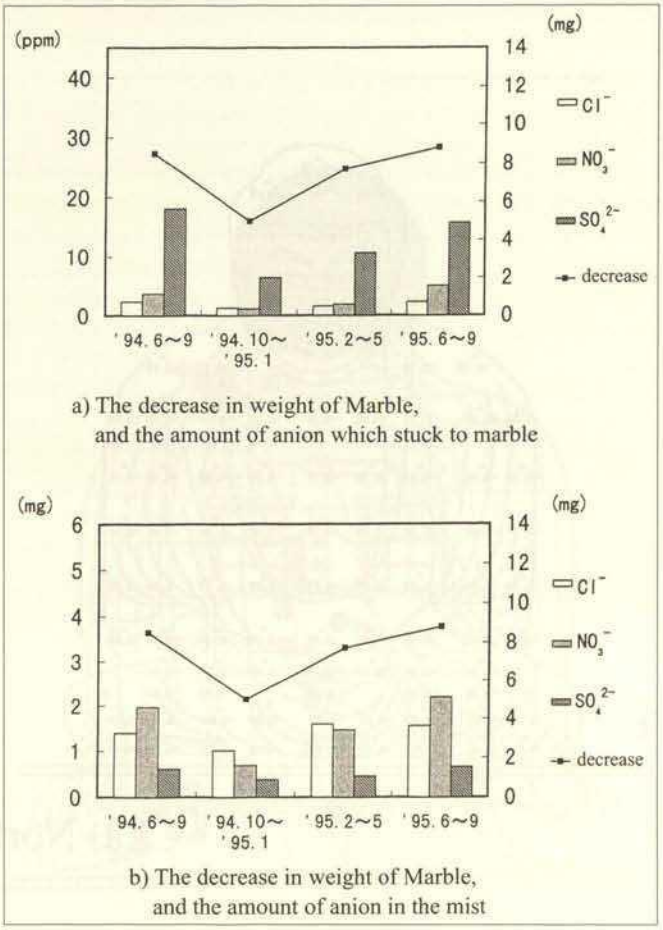

Fig. 6. The result of elution test of marble

Fig. 7. The appearance frequency of the direction of the wind seen at the time when it rained, and the strong wind

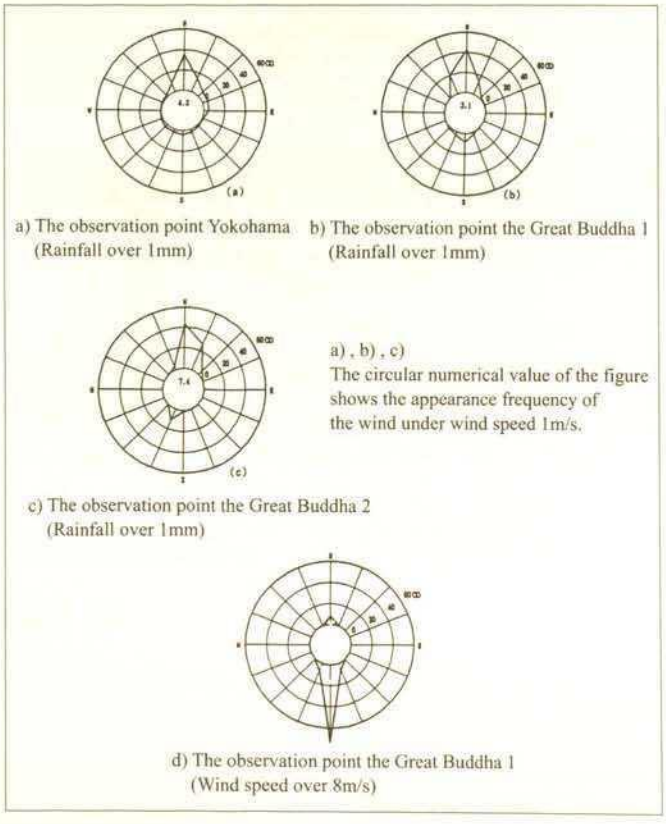

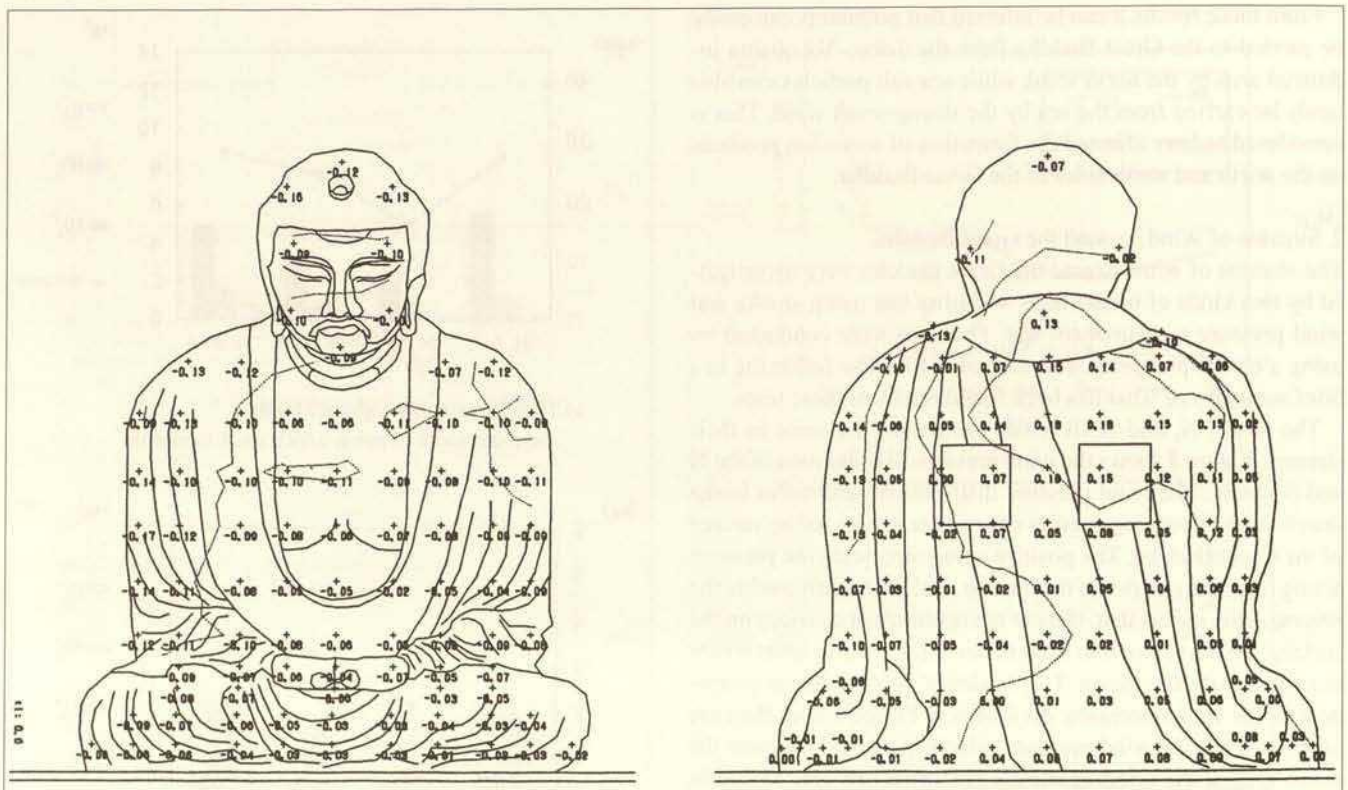

a) North wind

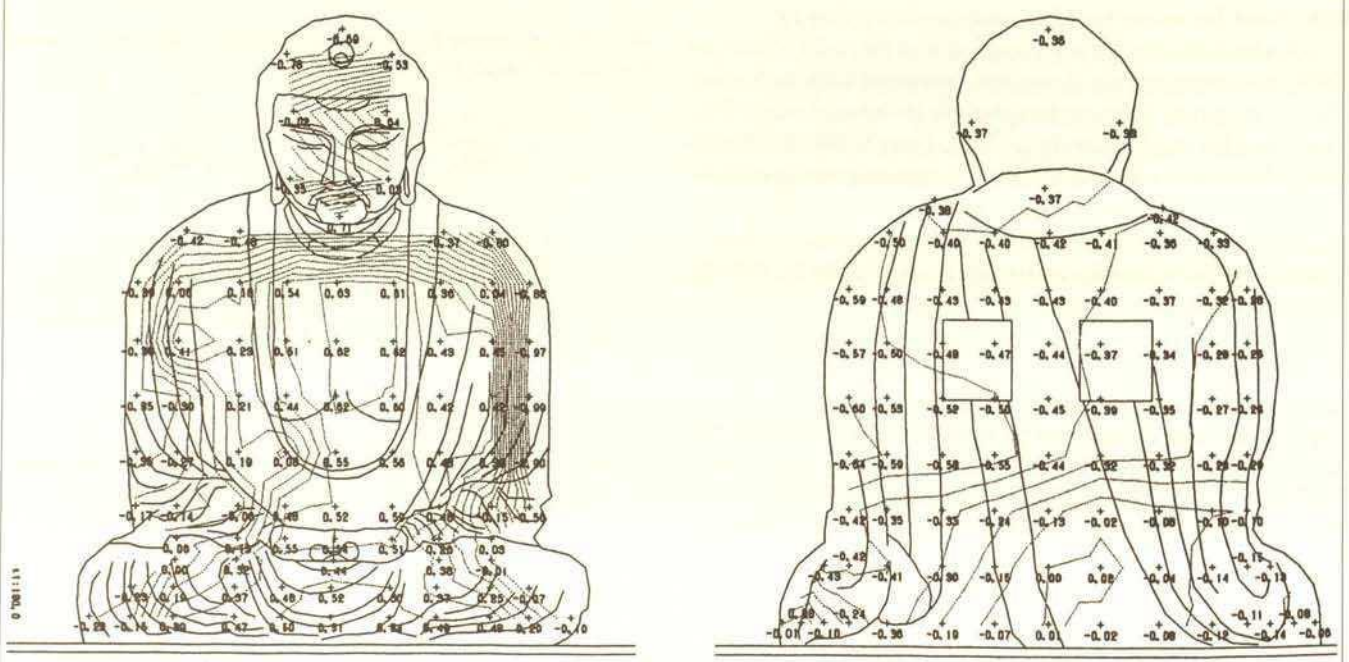

b) South wind

Fig. 8. The wind pressure force

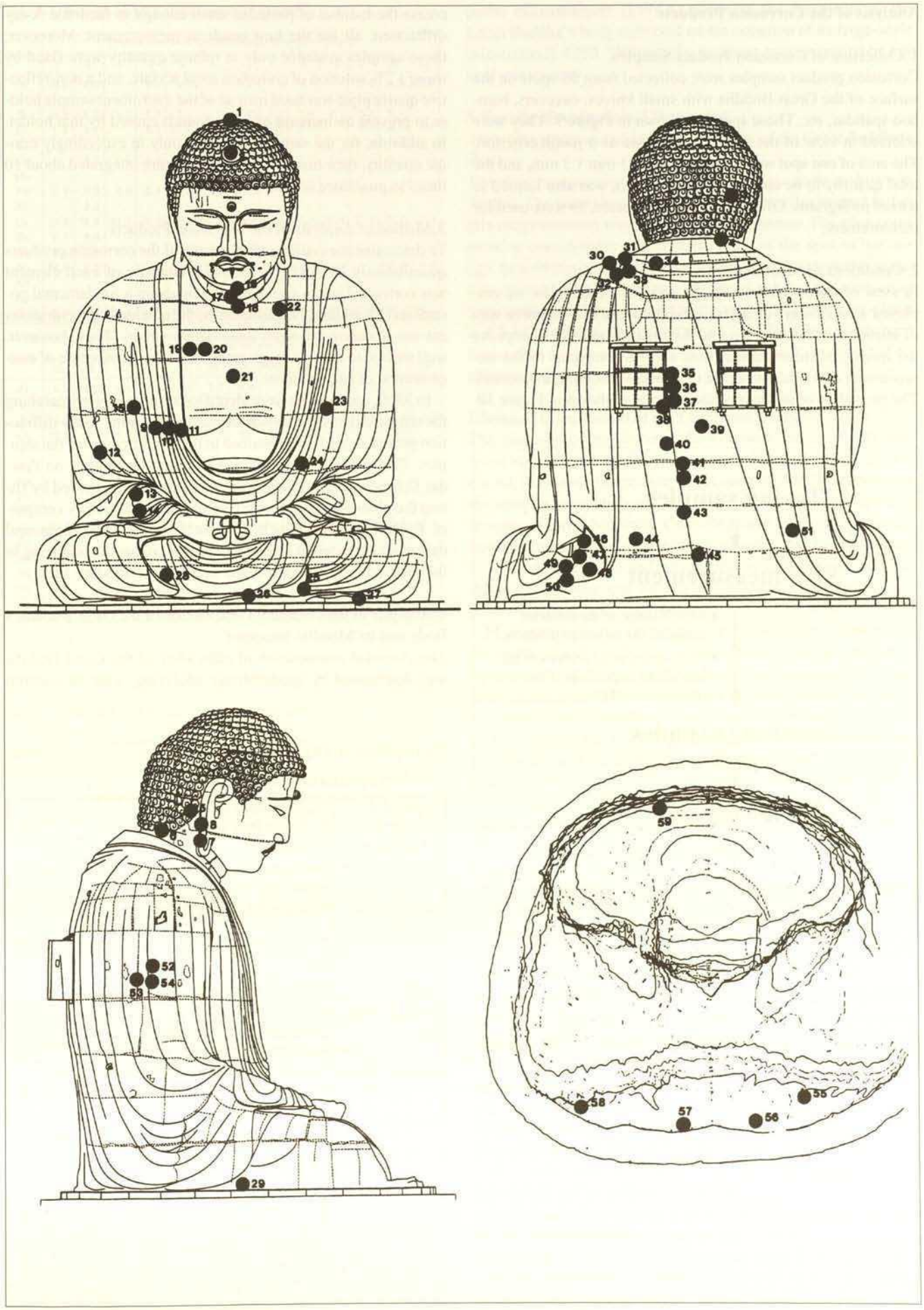

Fig. 9. The points where corrosion product samples were collected

Analysis of the Corrosion Products

1. Collection of Corrosion Product Samples

Corrosion product samples were collected from 59 spots on the surface of the Great Buddha with small knives, tweezers, bamboo spatulas, etc. Those spots are shown in Figure 9. They were selected in view of the surface color tone as a rough criterion. The area of one spot was limited to about 3 mm x 3 mm, and the total quantity to be collected from one spot was also limited to tens of milligrams. Of all the samples collected, 59 were used for measurement.

2. Conditions of Measurement

In view of the restrictions on the quantity of samples, we employed a lot of ways to devise an appropriate and effective way of introducing the samples into the instruments and to improve the quality of measurement (this can be compared to the improvement of a signal-to-noise ratio in electrocommunications). The procedure of analysis of the samples is shown in Figure 10.

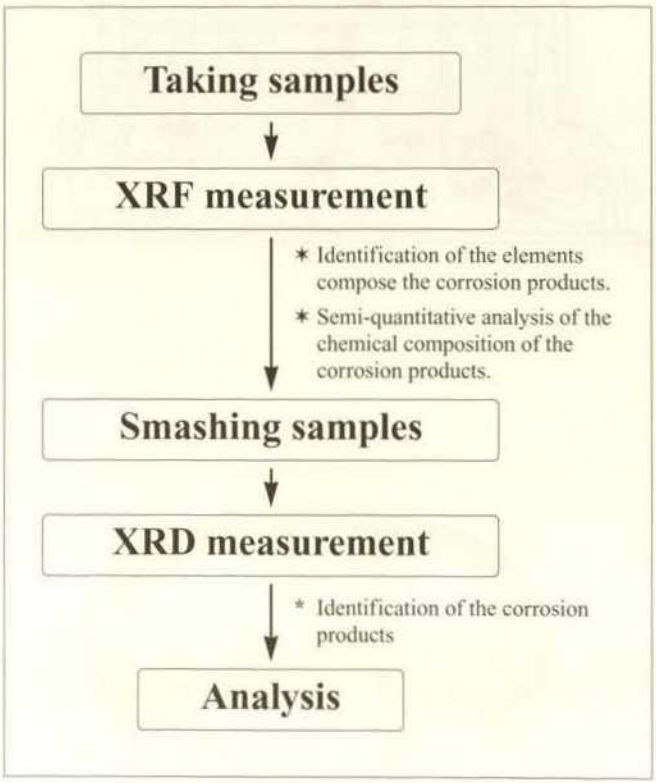

Fig. 10. The process of the analysis of corrosion product

First, the samples were analyzed by fluorescent X-ray spectroscopy (XRF), and the component elements of the corrosion products were identified. Their chemical composition was also determined semiquantitatively. They were then collected from the XRF sample holder and examined by X-ray diffraction (XRD). The conditions of measurement by XRF and XRD are shown in Table 3 respectively.

In XRF, fluorescent X-rays were absorbed by the Mylar film used to fix the samples. As a result, oxygen and other light elements could not be measured. Silicon could not be measured,either, because it is used as one of the materials of the sample holder.

In the measurement by XRD, those samples composed of large-sized particles were crushed up in an agate mortar to increase the number of particles small enough to facilitate X-ray diffraction, all for the best result in measurement. Moreover, those samples available only in minute quantity were fixed by using a 2% solution of collodion amyl acetate, and a non-reflective quartz plate was used instead of the instrument sample holder to prevent an increase of backgrounds caused by that holder. In addition, for the samples available only in exceedingly minute quantity, their measurement results were integrated about 10 times to guarantee accuracy.

3. Method of Analysis of the Corrosion Products

To determine the component elements of the corrosion products quantitatively by XRF, the detected intensity of each element was converted into a concentration by using a fundamental parameter (FP method). Consequently, the obtained concentrations are not accurate but semi-quantitative values. They, however, well suffice to make a rough estimate of the distribution of concentration of each element.

In XRD, compounds were identified respectively by searching the standard data for a substance that has the same X-ray diffraction pattern as each one obtained in the measurement of the samples. The standard data used was the Joint Committee on Powder Diffraction (JCPD) database. The data were retrieved by fitting the obtained measurement result to the database by computer. To facilitate the fitting by computer, the thinkable compound data were extracted in advance from the database by referring to the chemical composition of the samples analyzed by XRF.

4. Analysis of the Chemical Composition of the Great Buddha's Body and Its Metallic Structure

The chemical composition of each alloy of the Great Buddha was determined by quantitatively analyzing, with an electron

The conditions of XRF and XRD

Table 3. The conditions of XRF

Apparatus	Rigaku-denki co. 3270E
Elements	F - U (Except Si)
X-ray Energy	50kV/50mA
Sample holder	Sample were set on the high pure silicon wafer with mylar film.
Quantitative analysys	Fandamental Parameter

The conditions of XRD

Apparatus	Rigaku-denki co. Rotaflex RAD-rVB
X-ray Energy	45kV/150mA
Slit	Divergence : 1° Scatter : 1° Recieving : 0.3mm
Sample holder	Powdered samples were set on the non-refractive quartz holder with 2% collodion amyle acetate solution.

Table 4. The quatitative analysis by EPMA

No.	Sn	Pb	Fe	Al	Zn	As	Si	Ag	Cu
1	8.64	17.5	0.10	<0.01	<0.01	0.28	<0.05	0.09	bal.
2	12.9	16.4	0.01	<0.01	<0.01	0.52	<0.05	0.16	bal.
3	9.03	11.4	0.10	<0.01	<0.01	0.31	<0.05	0.05	bal.
4	7.36	11.6	0.12	<0.01	0.29-3.50*	0.04-0.26*	<0.05	0.05	bal.

*This mark shows that there is a difference in numerical value by the point that it was measured.

Table 5-1. Results of XRF measurement (1) (wt%)

Element	The point where corrosion product samples were collected (Fig.9)												
	1	2	3	4	5	6	7	8	9	10	11	13	14
Al	0.3	0.2		1.0	0.7		0.3	0.3	0.6		0.6	0.7	4.1
P	1.4	0.9		3.3	0.6	1.5	1.1	0.9	0.7	0.6	0.8	1.3	2.5
S	0.2	0.7	1.3	0.6	2.9	1.3	2.2	2.9	5.8	6.7	2.8	0.6	
Cl	1.8	5.1		6.2	10.6		3.1	9.9	2.0		6.3	4.0	2.0
K											1.9		
Ca		0.2	1.6	1.6	0.5	10.9	1.7	0.9	1.4	2.5	0.6	3.3	12.0
Mn											0.5		
Fe	2.9	0.8	3.0	2.4	1.9	3.9	1.1	0.6	1.3	1.6	1.7	6.5	17.5
Ni		3.3											
Cu	18.6	76.8	42.7	18.3	59.9	21.9	41.6	51.4	69.3	65.6	60.6	23.4	7.3
Zn	0.1	8.8											0.2
As	1.1												
Sn	24.9	0.5			1.1	16.3	10.3	1.8	1.7			12.0	3.4
Au								7.8					
Ag											1.0		
Pb	48.7	2.7	29.8	66.5	22.0	44.1	38.8	23.5	17.6	23.0	25.6	48.2	48.5

Element	The point where corrosion product samples were collected (Fig.9)												
	15	16	17	18	19	20	22	23	24	25	26	27	28
Al	0.3	0.3	0.4	1.5	1.1	1.7	0.8		1.0	0		1.2	
P	0.2	0.5	0.2		2.1	2.0	2.2	0.4	0.7			0.1	
S	1.6	1.6	0.3	1.0		1.4	1.0	1.9	2.6	1.3	1.2	0.4	0.5
Cl	12.1	12.1	16.3	26.6		12.9	6.2	7.5	6.9			1.5	
K												0.5	
Ca		0.4	0.5	1.1	3.7	3.4	1.0	1.1	1.4	2.9	2.1	10.0	1.9
Mn													
Fe	0.7	1.3	1.0	2.1	1.8	2.2	2.5	0.6	1.5			3.5	0.7
Ni													
Cu	61.4	51.2	77.4	57.7	54.0	55.7	27.4	83.1	63.4		1.4	64.3	12.6
Zn													
As													
Sn	1.9	3.1	3.9				1.0					0.9	
Au													
Ag													
Pb	14.5	29.5		9.9	37.3	20.5	58.0	5.5	22.5	95.8	95.2	17.5	84.3

Table 5-2. Results of XRF measurement (2) (wt%)

Element	The point where corrosion product samples were collected (Fig.9)												
	29	30	31	32	33	34	35	36	37	38	39	40	41
Al	1.1	1.1		0.5	0.5	0.3	0.2	5.8	2.2	0.1	2.6	1.0	4.6
P	0.2	2.5	4.9	2.2	1.5	1.0	0.7	0.5	2.1	0.2	1.7	0.7	0.5
S	2.5	0.7		0.4	0.2	0.2	3.1	0.7	0.2	2.6	0.7	2.5	0.7
Cl		4.3		2.4	1.4	4.0	0.9	0.9	3.2		3.0	2.6	0.7
K	0.2							3.2	1.4			0.6	2.3
Ca	6.1	4.5		5.7		0.8	3.3		3.8	6.1	3.1	1.3	6.1
Mn								0.4					0.3
Fe	2.6	4.8		1.9	2.2	1.1	0.7	20.7	9.9	0.6	8.9	5.2	17.8
Ni													
Cu	72.9	13.5	30.9	10.2	8.3	18.9	50.0	32.2	23.1	43.3	26.0	56.1	40.1
Zn								0.2			0.2		
As					1.6		1.1			1.9			
Sn	0.5			18.3	34.7		11.6	3.9	1.7	22.5	2.9	1.9	5.5
Au													
Ag										0.4			
Pb	13.8	68.6	64.2	58.5	49.6	73.8	28.4	31.5	52.4	22.1	51.1	28.1	21.4

Element	The point where corrosion product samples were collected (Fig.9)												
	42	43	44	45	46	50	51	52	53	54	56	58	59
Al	2.0	1.1		4.3	0.9	3.0	0.5	3.2	0.5	2.4	0.2	0.4	0.1
P	0.2	0.4	0.3		0.6	1.3	0.4	0.4		0.7	0.2	0.1	0.2
S	1.4	1.1	3.8	0.4	7.6	1.4	2.6	1.3	3.6	1.5	0.6	1.8	0.6
Cl	0.6	1.5	3.2	1.0		2.8	3.3	2.5	2.0	3.1	11.5	15.9	2.1
K	0.5				8	1.8		1.9		1.3			
Ca	3.8	2.8				3.9		3.8	4.6	4.4		0.8	5.5
Mn					3.8								
Fe	3.7	7.5	0.6	7.2		55.9	1.6	10.6	1.6	8.1	0.3	0.7	1.0
Ni				31.6									
Cu	50.6	52.3	32.6	33.5	10.0	15.2	60.2	45.1	55.8	46.5	61.5	59.0	31.5
Zn				0.5				0.5	0.2				
As	0.8								1.8				0.7
Sn	20.6	10.4	13.3	9.1			8.8	2.8	7.8	5.6	14.5	1.6	17.2
Au													
Ag													0.5
Pb	15.6	22.8	46.3	12.4	77.1	15.2	22.5	27.8	22.0	26.4	11.2	19.8	40.7

probe microanalyzer (EPMA), some of the fragments of the Great Buddha's body collected on the occasion of its large-scale restoration in 1960. The metallic structure was examined by optical microscopy.

5. Results of Analysis and Discussion

Alloy Composition and Metallic Structure of the Great Buddha's Body

The alloy composition of the Great Buddha's body is shown in Table 4. The most remarkable characteristic in this respect is that this image contains more Pb than normal bronze. The alloy composition considerably varies, depending on the spot of the image. In conformity with the alloy composition, its metallic structure consists of three different phases: α-solid phase containing a comparatively large amount of Cu, eutectoid phase of α-phase and δ-intermetallic compound phase, and Pb phase. It has been found that the Pb phase is minutely dispersed between the α-phase and the eutectoid phase.

Chemical Composition of the Corrosion Products

The chemical composition of the corrosion products was analyzed by XRF and its result is shown in Table 5. Cu, Pb, Sn, Fe, Ca, Al, S, Cl, and P were detected in over 80% of the spots where the samples were collected. Au, Ag, As, etc. were also detected in some of them. Naturally, Cu is the major metal component in terms of quantity. Another distinct feature is that the Pb content is noticeably high. Ca and Al can be considered to derive from the soil component that was carried by the wind, while S and Cl from the atmospheric environment.

Most striking in the distribution of the component elements of the rust are S and Cl. That is, on the whole, S is more concentrated especially at the rear (north side) of the image, and Cl on the front (south side). This is considered to be related to the conditions of the Great Buddha's location as it stands facing the shore on its front and the Tokyo-Yokohama industrial area on its rear. The reason will be examined comprehensively in more detail when the results of our meteorological observations (such as rainfall and wind direction) now under way and the result of analysis of rainwater become available.

P was detected on the entire surface of the image. This cannot be considered to derive from the soil or atmospheric environment in the neighborhood. Its most probable source is droppings from doves and other birds that used to fly to the neighborhood of Kotoku-in Temple in flocks.

Distribution of the Corrosion Products

By taking into account what was found about the chemical composition of the corrosion products as described in the preceding section, the structures of the corrosion products were identified on the basis of the measurement result by XRD. The result of analysis was classified into three grades of reliability from high to low according to the criteria as shown in Table 6. The result of analysis is shown in Table 7. To make this result easier to understand, the corrosion products were further classified according to the compounds composed of Cu, Pb, and Sn. The following has been found from Tables 6:

1. Copper compounds:

– Brochantite: Brochantite was found to be the most principal patina component. It was detected in 63% of the spots where the samples were collected. It is distributed uniformly over the entire surface of the image and has no special features in

Table 6. Criteria for the result of analysis by XRD

Determination	Evaluation items	
	Degree of coincidence with the diffraction pattern	Comparison with the composition (by FXR)
High reliability	High	In agreement
Middle reliability	High	Slightly different
	Middle	In agreement
Low reliability	High	Different
	Middle	Slightly different
	Low	In agreement

this respect. By judging from the result described in the preceding section, brochantite is considered to exist in a greater amount on the front (south side) of the image than at the rear (north side).

- Malachite: Malachite, also a patina component, was detected in 21% of the sample collection spots. It was always accompanied by brochantite. This suggests that malachite, which had originally stayed stable, came to be transformed into brochantite in recent years.
- Antlerite: Antlerite was detected in two spots on the rear (north side) and in one spot on the west side. It was not detected at all on the south side (the front) and the east side. This suggests that the north (the rear) and the west sides are exposed to the bitter strong acid environment.
- Atacamite: Atacamite was detected in 45% of the sample collection spots and shows a tendency to exist in a greater amount on the front (south side). This is considered to be related to the fact that the Great Buddha's front faces the shore.
- Copper oxides: Copper oxides were detected in over 80% of the sample collection spots as cuprous oxide. As a general rule, the cross section of a rust layer on copper is considered to have a structure of layers consisting of Cu_2O, CuO, and patina from internal to external. In our study, both cuprous copper and patina were detected at the same time in almost all the sample collection spots. This result can well be understood by presuming that almost all the rust layers on the Great Buddha have a two-layer structure consisting of oxide (internal layer) and patina (external layer).

2. Lead compounds:

Lead compounds were detected in over 80% of the sample collection spots. They are mainly lead sulfate, basic lead phosphate, chlorolead phosphate, and lead carbonate. Of these, lead sulfate and chlorolead phosphate are present in greater amounts. On the whole, the former is distributed more at the rear (north side), while the latter more on the front (south side). This is considered to be due to the conditions of the Great Buddha's location as in the case of copper alloys. In addition, metallic lead, which flaked off the Great Buddha's body, was detected on the base and lower parts of the image.

3. Tin compounds:

Tin compounds were detected in 30% of the sample collection spots mainly as oxides. Besides, tin can be considered to be

Table 7-1. Results of XRD measurement (1)

Point (Fig.9)	Color	High reliability	Middle reliability	Low reliability
1	Pale Green	Cu_2O	$CaCO_3$, SnO_2	CuBr, $AlPO_4$, SnO PbO_2, $PbAs_2O_6$ Al_2SiSiO_5
2	Dark Brown	Cu_2O	$Cu_2Cl_4(OH)_{10}\cdot H_2O$ (Atacamite) CuO	Zn_2SnO_4, $Cu_{0.8}Sn$ CuZn, Cu_2ZnSiS_4 $CuCl_2\cdot 3Cu(OH)_2$
3	Pale Green	Cu_2O, $Cu_4(OH)_6SO_4$ $Cu_4SO_4(OH)_6$	$Pb_5(PO_4)_3Cl$, SnO_2	$PbSO_4$, SnO, CuCl $CuCO_3$
4	Black	$Pb_5(PO_4)_3Cl$	Cu_2SO_4	Cu_2O, $Cu_4SO_4(OH)_6$ (Brochantite) $CuCl_2\cdot 3Cu(OH)_2$ $Cu_2(OH)_3Cl$ (Paratacamite) Al_2SiSiO_5
5	Dark Green	Cu_2O, $Cu_2(OH)_3Cl$ $Cu_4(OH)SO_4$ (Brochantite)	$CuCO_3\cdot CU(OH)_2$ (Malachite) $Pb_5(PO_4)_3OH$ $Pb_5(PO_4)_3Cl$	$CuSO_4\cdot H_2O$ $FeCO_3$ $SnCl_4$, $Cu_{1.96}S$, $Cu_{7.2}S_4$
6	Pale Green	$Pb_5(PO_4)_3Cl$	$Cu_4SO_4(OH)_6$ (Brochantite) $PbSO_4$, $CaSO_4$	Cu_2O, Fe_2O_3, Sn, SnO Sn_3O_4
7	Pale Green	$Cu_4SO_4(OH)_6$ $Cu_4(OH)_6SO_4$ (Brochantite)	$Pb_5(PO_4)_3Cl$ $Cu_2Cl(OH)_3$	CuCl, $PbFe_2O_4$ $CaCO_3$
8	Yellow (Surface) Blue (Inside)	$Cu_4SO_4(OH)_6$ $Cu_4(OH)_6SO_4$ $Cu_2Cl_4(OH)_{10}\cdot H_2O$ $Pb_5(PO_4)_3Cl$, Au	Cu_2O $CuCO_3\cdot Cu(OH)_2$ (Malachite)	CuCl, $PbFe_2O_4$ $CaCO_3$
9	Pale Green	$Cu_4SO_4(OH)_6$ $Cu_4(OH)_6SO_4$ (Brochantite) $Pb_5(PO_4)_3Cl$	Cu_2Cl $FeSO_4$	Cu_2O, Fe_2O_3, Fe_3O_4 Pb_2CuCl_2
10	White	Cu_4O, $Cu_4SO_4(OH)_6$ $Cu_4(OH)_6SO_4$ (Brochantite)	$PbSO_4$ $Cu_2Cl_4(OH)_{10}\cdot H_2O$ (Atacamite)	$CaSO_4$, $FeSiO_3$ $CaSIO_3$
11 12	Dark Green	$Cu_4SO_4(OH)_6$ $Cu_4(OH)_6SO_4$ (Brochantite) $Pb_5(PO_4)_3Cl$	Cu_2O	$Cu_2Cl_4(OH)_{10}H_2O$ (Atacamite) $Cu_2CO_3\cdot Cu(OH)_2$ (Malachite) $Pb(PO_3)_2\cdot H_2O$, $CaCO_3$
13	Yellowish Green	$Su_4SO_4(OH)_6$ $Cu_4(OH)_6SO_4$ (Brochantite) $Pb_5(PO_4)_3Cl$	Cu_2O $Cu_2Cl_4(OH)_{10}\cdot H_2O$ (Atacamite) SnO	$Cu_2CO_3\cdot Cu(OH)_2$ (Malachite) Cu_2Cl, $FeSO_4$, $CaCO_3$
14	White		$Pb_5(PO_4)_3OH$, $Fe(OH)_3$, $CaAl_2O_4$	SiO_2, $AlPO_4$, Cu_2O FeOOH, $CuCl_2$, Fe_2SiO_4 $Cu_2Pb_3(SO_4)_2CO_3(OH)_4$ Al_2SiO_5

Table 7-2. Results of XRD measurement (2)

Point (Fig.9)	Color	High reliability	Middle reliability	Low reliability
15	Green	$Cu_4Cl(OH)_6$ (Atacamite) Cu_2O, $PbSO_4$	$CuPb_3(PO_4)(SO_4)(OH)$ $Cu_2Cl_4(OH)_{10}\cdot H_2O$ (Atacamite)	$Pb_5(PO_4)_3$, Fe_2O_3 $Cu_4SO_4(OH)_6\cdot H_2O$ (Posnjakite) $Cu_4SO_4(OH)_6$ (Brochantite)
16	Pale Green	Cu_2O, $PbSO_4$	$Cu_2Cl(OH)_3$ (Atacamite) $Cu_2Cl_4(OH)_{10}\cdot H_2O$ (Atacamite)	CuCl, Cu_2S, FeOOH Sn_3O_4, SiO_2 $2PbCO_3\cdot Pb(OH)_2\cdot H_2O$
17	Dark Green	Cu_2O $Cu_2Cl_4(OH)_{10}\cdot H_2O$ (Atacamite)	$CuSO_4(OH)_6$ (Brochantite) $CuCO_3\cdot Cu(OH)_2$ (Malachite) $(CuZn)_2(CO_3)(OH)_2$	$CuCl_2$, $CaCO_3\cdot H_2O$ Sn_3O_4
18	Yellowish Green	$Cu_2Cl_4(OH)_{10}\cdot H_2O$ (Atacamite) $Cu_2Cl(OH)_3$ (Paratecamite)	Cu_2O, $PbCO_3$	$CuSO_4\cdot H_2O$ $FeSO_4\cdot 5H_2O$, Al_2O_3 $CaSiO_3$
19	Pale Green	Cu_2O	$CuSO_4(OH)_6$ $Cu_4(OH)_6SO_4$ (Brochantite) $Pb_5(PO_4)_3Cl$ $PbFe_2O_4$	$Pb_5(PO_4)_3OH$, $CaCO_3$ Al_2SiO_5
20	Yellowish Green	Cu_2O, $Pb_5(PO_4)_3Cl$ $Cu_2Cl(OH)_3$ (Atacamite)	$Pb_5(PO_4)_3OH$ $Pb(FeCuAl)_3(SO_4)_2(OH)_6$	$PbSO_4$, Pb, $CaCO_3$ $Cu_2Cl_4(OH)_{10}\cdot H_2O$ (Atacamite) $Cu_2Pb_3(SO_4)_2CO_3(OH)_4$
21	Dark Brown	Cu_2O $Pb_5(PO_4)_3Cl$	$Cu_2(OH)_3Cl$ (Paratacamite) $Cu_2Cl_4(OH)_{10}\cdot H_2O$ (Atacamite) $Cu_4SO_4(OH)_6$ $Cu_4(OH)_6SO_4$ (Brochantite)	$PbFe_2O_4$, $CaSiO_3$, Sn
22	Dark Brown	$Pb_5(PO_4)_3Cl$	Cu_2O, $Pb_3O_4CO_3$ $Cu_4SO_4(OH)_6$ (Brochantite) $Pb_5(PO_4)_3OH$	PbO_2, FeO, SnO $Cu_2Cl(OH)_3$
23	Green (Surface) Redish Brown (Inside)	Cu_2O $Cu_4SO_4(OH)_6$ (Brochantite)	$PbSO_4$ $Cu_2Cl_4(OH)_{10}\cdot H_2O$	FeS, FeOOH, $CaSO_4$ PbO, $Pb_5(PO_4)_3Cl$
24	Black	Cu_2O $Cu_4(OH)_6SO_4$ (Brochantite)	$Pb_5(PO_4)_3Cl$ $Cu_2Cl(OH)_3$	CuO, CuCl, PbO FeOOH, $SnCl_4$, $CaCO_3$ $FeSO_4$
25	White	Pb_{12}, $Pb_3(CO_3)_2(OH)_2$ $Pb_4(SO_4)$ $(CO_3)_2(OH)_2$	$PbSO_4$	$Pb_{12}(CO_3)_8(OH)_4O$ $CaCO_3$
26	White	Pb, $PbCO_3$	$PbSO_4$ $Pb_3(CO_3)_2(OH)_2$	PbO, PbClOH, $CaCO_3$ CuO

Table 7-3. Results of XRD measurement (3)

Point (Fig.9)	Color	High reliability	Middle reliability	Low reliability
27	White	$Cu_2CO_3(OH)_2$ (Malachite) $CaCO_3$	$FeSO_4 \cdot H_2O$, FeS $SnCu(PO_4)_2 \cdot 3H_2O$	Cu_2O, $Pb_3(CO_3)_2(OH)_2$ $Ca_4Al_2(OH)_{12}SiO_4$ $Cu_4(OH)_6SO_4$ (Brochantite)
28	White	Pb, $Pb_3(CO_3)_2(OH)_2$	PbO, PbO_2	Cu_2O, Cu_2O_3, Cu_2S, FeOOH $2PbCO_3 \cdot Pb(OH)_2$
29	White	$Cu_4SO_4(OH)_6$ $Cu_4(OH)_6SO_4$ (Brochantite)	$Cu_3(SO_4)(OH)_4$ (Antlerite) Cu_2O, Al_2SiO_5	SiO_2, $CaSO_4$ $Cu_2Al(SO_4)Cl(OH)_{12} \cdot 3H_2O$
30	Red Black	$Pb_5(PO_4)_3Cl$ $Pb_5(PO_4)_3OH$	$PbSO_4$	FeOOH, Cu_2O, $PbCO_3$ $Cu_4(OH)_6SO_4$ (Brochantite) $CaCO_3$, Pb_2O_4, PbO_2 $CuCl_2 \cdot 2H_2O$
31	Red Black	CuO, Cu_2O	$Pb_5(PO_4)_3Cl$, $CuPO_4$ $Cu(PO_3)_2$	PbO_2, SiO_2, CuCl
32	Yellowish Green	$Pb_5(PO_4)_3Cl$	SnO, CuO	$Cu_2Cl_4(OH)_{10} \cdot H_2O$ (Atacamite) $CaCO_3$, Al_2SiO_5
33	Green	$Pb_5(PO_4)_3Cl$		CuO, $CuCO_3$, Fe_2CO_3 $PbSO_4$
34	Red Black	PbO, $Pb_5(PO_4)_3Cl$	$Pb_3(CO_3)_2(OH)_2$ $PbCO_3$, SiO_2	$Cu_2(OH)_3Cl$ (Atacamite) CuCl, Pb, PbO_2
35	Pale Green	CuO, $Pb_5(PO_4)_3Cl$ $Cu_4SO_4(OH)_6$ $Cu_4(OH)_6SO_4$ (Brochantite)	SnO	Cu_2Cl, $CaCO_3$, CuCl
36	Red White	$PbSO_4$	Al_2SiO_5, PbO $Cu_4(OH)_6SO_4$ (Brochantite) $Pb_2Cu(CO_3)(SO_4)$	$Cu_2Cl(OH)_3$ SiO_2 $PbSO_4$, Sn_6O_8, $FeAl_2O_4$
37	Brown (Porous)	Al_2SiO_5	$PbSO_4$, $Cu_4SO_4(OH)_6$ $Cu_4(OH)_6SO_4$ SiO_2, $CuPO_4$	$Cu_2CO_3(OH)_2$ $Cu_2Cl_4(OH)_{10} \cdot H_2O$ $KFe(SO_4)_2$, $CaCO_3$
38	Pale Green	$Cu_4SO_4(OH)_6$ $Cu_4(OH)_6SO_4$ (Brochamtite)	Cu_2O, $Pb_5(PO_4)_3Cl$ Sn_3O_4 $Ca_3Pb_2(OH)_2$ $(SO_4)_2Sn_6O_{14}$	CuO, PbSO, $Cu_2Cl(OH)_3$, SnO SnO_2 (Amorphous?)
39	Brown (Porous)	$Pb_5(PO_4)_3Cl$ SnO_2	$Pb_5(PO_4)_3OH$ SiO_2, Al_2SiO_5 $3CuO \cdot SO_3 \cdot 2H_2O$ (Antlerite)	$CuCO_3$, $GaFe_2O_4$ $CaAl_2Si_2O_8$ $Ca_3Al_2Si_4O_{16}(OH)_4$
40	Dark Green	$Pb_5(PO_4)_3Cl$ $Cu_4SO_4(OH)_6$ $Cu_4(OH)_6SO_4$ (Brochntite)	$Cu_2Cl(OH)_3$, Cu_2O $CuSO_4 \cdot H_2O$	$PbAl_2SiO_6$ $Sn_{10}Cl_{14}(OH)_{12}O_4$

Table 7-4. Results of XRD measurement (4)

Point (Fig.9)	Color	High reliability	Middle reliability	Low reliability
41	Brown	$CuCO_3 \cdot Cu(OH)_2$ (Malachite) Al_2SiO_5, SiO_2	$K_2Al_2O_3(CO_3)_2 \cdot 2.4H_2O$ $FeSiO_3$	K_4CuCl_4, $Ca_3(PO_4)_2$ $Ca_2Si_2O_7$
42	Green	Cu_2O	SiO_2, $Cu_3(PO_4)_2$ $Cu_2Cl_4(OH)_{10} \cdot H_2O$ (Atacamite) $Cu_4SO_4(OH)_6$ $Cu_4(OH)_6SO_4$ (Brochantite)	$CuCl_2 \cdot 3[Cu(OH)_2]$ $Cu_2CO_3(OH)_2$ (Malachite) $Cu_{0.8}Sn$ $K_4CuCl_4 \cdot 2H_2O$
42	Green	Cu_2O	$CuCl_2 \cdot 3[Cu(OH)_2]$ $Cu_4(OH)_6SO_4$, SiO_2 $Fe_2O_3 \cdot 1.2H_2O$ $K_4CuCl_4 \cdot 2H_2O$	SnO, $Cu_{4.4}Sn$
43	Gray	$Cu_4SO_4(OH)_6$ $Cu_4(OH)_6SO_4$ (Brochantite)	$Cu_2CO_3(OH)_2$ (Malachite) $Pb_5(PO_4)_3Cl$	Cu_2O, $PbSO_4$ $Cu_2Cl(OH)_3$ Al_2SiO_5
44	White	Cu_2O, $PbSO_4$ Pb_3O_4	$Cu_2Cl(OH)_3$ $Cu_4(OH)_6SO_4$	SiO_2, SnO, CuCl, Fe_2O_3
45	Red	SiO_2, $PbSO_4$, Cu_2O $Cu_4(OH)_6SO_4$	Al_2SiO_5 $(CuZn)_3(SO_4)_2(OH)_{10} \cdot 3H_2O$	Cu_2S_2, C
46	White	$PbSO_4$	PbO_2, Cu_2O, $Al(OH)_3$	$Pb(OH)_2$ $Pb_3(CO_3)_2(OH)_2$ Ca_2CuO_3, Pb_3CO_5
47	Green	$PbSO_4$ $Cu_4SO_4(OH)_6$ $Cu_4(OH)_6SO_4$ (Brochantite)	Cu_2O, $Cu_2Cl(OH)_3$ $Cu_2(OH)_3Cl$ (Paratacamite) $Cu_2Cl_4(OH)_{10} \cdot H_2O$ (Atacamite) $FeCl_2 \cdot 2H_2O$	PbCl(OH), SnO, SnO_2 $CaSiO_3$
48	Yellow	Cu_2O, PbSO, $Cu_2Cl_4(OH)_{10} \cdot H_2O$ (Atacamite)	$Cu_2CO_3(OH)_2$ (Malachite)	FeS, $Cu_2(OH)_3Cl$ $Pb_2O(PO_4)_2$ $Pb_5(PO_4)_3OH$, Pb
49	Green oral Brown (layer)	Cu_2O, $PbSO_4$	$Cu_2Cl_4(OH)_{10} \cdot H_2O$ (Atacamite) $Cu_2Cl(OH)_3$ (Atacamite) Pb_2SiO_4	SiO_2, $Al(OH)_3$, $CaSO_4$
50	Red	Pb, Cu_2O, $PbSO_4$	Al_4O_3, C $Cu_2CO_3(OH)_2$ (Malachite)	Fe_2O_3, Fe_3O_4 $FeCl_2 \cdot H_2O$ $Cu_2Cl_4(OH)_{10} \cdot H_2O$ (Atacamite) $Cu_4(OH)_6SO_4$ (Brochantite)
51	Black	$PbSO_4$, Cu_2O $Cu_4(OH)_6SO_4$ (Brochantite)	$Cu_2Cl(OH)_3$ (Atacamite)	$SnCl_4$, Sn_2S_3, C $Cu_2Cl_4(OH)_{10}$
52	Black	SiO_2 $Cu_4(OH)_6SO_4$ (Brochantite)		Cu_2O, $FeSiO_3$, $CaAl_2O_4$ $CaAl_2Si_2O_8$ $Pb_5(PO_4)_3OH$

Table 7-5. Results of XRD measurement (3)

Point (Fig.9)	Color	High reliability	Middle reliability	Low reliability
53	Pale Green	Cu_2O, $Cu_4SO_4(OH)_6$ $Cu_4(OH)_6SO_4$ (Brochantite)	FeS, $FeCl_3 \cdot H_2O$ C, PbS	$Cu_2Cl_4(OH)_{10} \cdot H_2O$ (Atacamite) SnZnAs, Pb
54	Black (Snrface) Pale Green (Inside)	Cu_2O	SnO_2, SiO_2 $Cu_2Cl(OH)_3$ (Atacamite) $Pb_5(PO_4)_3OH$	$CuCl_2$, Si, $CaAl_2Si_2O_8$ K_2SnO_4
56	Green	$Cu_2Cl_4(OH)_{10} \cdot H_2O$ (Atacamite) $CuCl_2 \cdot [Cu(OH)_2]$	CuCl, $PbSO_4$, SnO	$Cu(OH)Cl$, Pb_3CO_5 Sn_3O_4, $CaCuO_2$ $Ca_2SiO \cdot H_2O$
58	Green	$PbSO_4$ $Cu_2Cl_4(OH)_{10} \cdot H_2O$ (Atacamite)	Cu_2O, $Fe_3(PO_4)_2$	$CaSiO_3$, Fe_2O_3, Al_2O Al_2SiO_5
59	Green	$PbSO_4$	Cu_2O, $Pb_3(CO_3)_2(OH)_2$	$Cu_2CO_3(OH)_2$ (Malachite) $Cu_4(OH)_6SO_4$ (Brochantite) $CaCO_3$, $FeCO_3$ $Fe(PO_3)_2 \cdot H_2O$

present as complex components of patina. However, the amount of tin as corrosion products on the image is comparatively small.

4. Other compounds:
Aluminum silicate (a soil component) and quartz, among other compounds, were detected in 80% of the sample collection spots. They are considered to be part of the grains of sand that flew to the image and adhered to its surface together with corrosion products. Iron rust was also detected in some of the spots.

5. Conclusion

To conserve the Great Buddha in Kamakura properly, a wide range of studies was conducted: measurement of various environmental pollutants that are considered to have been affecting the image, observation of the directions of wind that carries those pollutants, and analysis of the corrosion products on the surface of the image. The results can be summarized as follows:

1. The distribution of rust and its change on the surface of the Great Buddha were studied by performing computer image processing of color photographs taken in 1965, 1985, and 1994. As a result, it was found that a greater change had taken place in the 20 years from 1965 to 1985 than in the years from 1985 to 1994. The years around 1965 were a period when the emission of sulfur dioxide and other environmental pollutants was a serious problem. The drastic change in this period is also in agreement with the eyewitness account by the chief priest of Kotoku-in Temple. The light conditions at the time of shooting and the scaling of rust tones were difficult problems for the image processing of the photographs, but image processing has been found to be an important non-destructive way of examination.

2. As a result of our meteorological observations, it has been found that the wind blows mainly from the north in and around Kamakura. Especially in case of 1 mm or more of rain, almost all the wind is from the north. Strong winds of 8 m/s or more, however, are often from the south. From these facts it can be inferred that pollutants are carried to Kamakura by the north wind from the Tokyo-Yokohama industrial area, a huge emission source of environmental pollutants, and that sea salt particles are carried from the sea by the strong south wind. Naturally, all this is considered to have an effect upon the gen-

eration of corrosion products on the north and south sides of the Great Buddha.

3. By taking the observation data of the wind into account, the streams of wind around the Great Buddha were examined by wind tunnel tests. The north wind was found to blow against the rear of the image, thereby producing positive wind pressure on almost the entire area of its rear, which in turn causes rain of low pH in the initial stage of a rainfall to be permeated deeply into the rust layer formed on the image. The result of our wind tunnel tests is in agreement with the distribution of antlerite, which is considered to be generated by acid rain.

4. In the analysis of the corrosion products, sulfate patina mainly composed of brochantite was detected on the entire surface of the Great Buddha. Its amount was greater at the rear.

5. Antlerite was detected on the rear and left side of the Great Buddha. This is in agreement with the result of the wind tunnel tests.

6. A great amount of atacamite, a kind of chloride patina, was detected on the front of the Great Buddha. This is in agreement with the result of the wind tunnel tests.

7. Malachite, a kind of carbonate patina, was always detected together with brochantite. It can, therefore, be inferred that some the of old malachite was transformed into brochantite due to the effect of environmental pollutants.

8. The corrosion products of lead, an alloy component of the Great Buddha, were detected in large amounts on the entire surface.They are mainly chlorophosphate on the front and sulfate at the rear.

9. The amount of the corrosion products of tin was comparatively small. This is in agreement with the result that Sn was scarcely eluted in the elution test of the bronze plate.

Literature

Robert Baboian/E. Lawrence Bellante/E. Blaine Cliver, *The Statue of Liberty. Restoration,* in: NACE International, New York 1986.

Shirou Matuda, *Corrosion and that Anticorrosion,* in: Institute of Sumitomo Maining, 1991.

Shirou Matuda/Shigeo Aoki, *Analysis of Corrosion Products Formed on the Great Buddha Image of Kotoku-in Temple in Kamakura,* in: Conservation Science 35, 1996.

Photo Credits

All figures by the authors